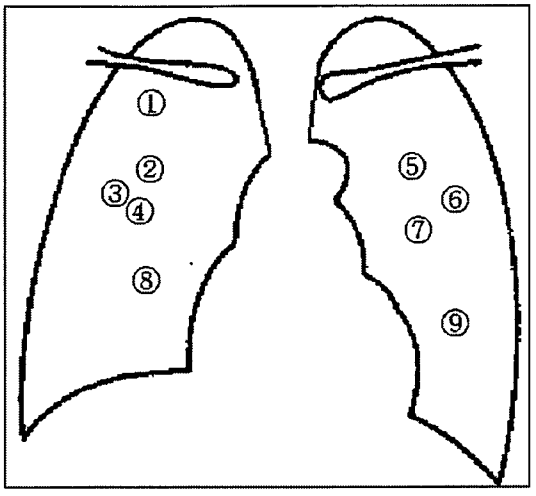

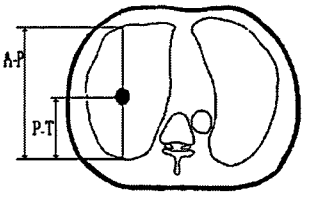

case	location	P-T/A-P
1	Right upper	5.1/12.
2	Right upper	3.0/12.
3	Right upper	5.2/12.
4	Right upper	9.3/16.
5	Left upper	11./14.
6	Left upper	2.0/13.
7	Left upper	7.5/12.
8	Right middle	4.0/17.
9	Left lower	8.6/13.

Figure 1 Locations of the nine lesions evaluated in this study. The table on the right indicates the tumor position in the antero-posterior direction. P-T: distance from the posterior margin of the lung to the center of tumor on an antero-posterior line through the center of the tumor on an axial CT plane that includes the tumor. A-P: distance between the anterior and posterior margin of the lung on the same line.

relatively small, minimal field sizes of 4 cm by 4 cm were employed.

Beams of 6-MV photon generated from the linear accelerator (ML15-MV, Mitsubishi Electric Co., Tokyo, Japan) were used. Dose calculations were carried out to deliver 12 Gy at the isocenter, and the all static beams or arcs were weighted equally at the isocenter. In that condition, the sum of the monitor unit (MU) for all beams required to give 12 Gy at the isocenter was recorded and the doses at the isocenter were rescaled to the doses when 100 MU were used for the total of the dose delivery (i.e. the rescaled isocenter dose = 12 (Gy) × 100 (MU)/ the sum of monitor unit for all beams). Two dose calculation algorithms, the Fast Fourier Transform (FFT) convolution and the multigrid (MG) superposition [17] based on a convolution and a superposition algorithms [15,16], were used.

Path-length and effective path-length

Relative electron density maps were generated from CT data and a calibration curve that had been previously obtained from CT scanning of a calibration phantom. Path-lengths, L, and effective path-lengths, L_{eff} were calculated with pixel-by-pixel integration of values from the relative electron density map through the beam path, from the incident point of the beam center-line to the isocenter at the center of the tumor. Mean path-length, $\bar{L}$ and mean effective path-length, $\bar{L}_{eff}$ for Static Irradiation were calculated from values obtained by various beams, i, according to the following equations:

$$\bar{L} = \sum_{i=1}^{n} L_i/n \quad (1)$$

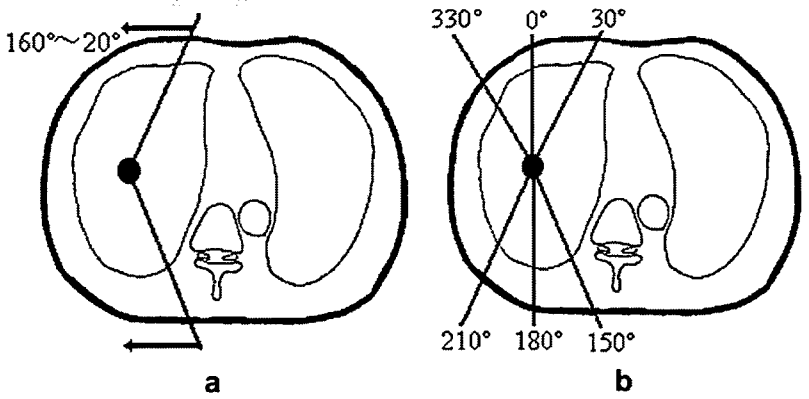

Figure 2 Beam configurations. (a) Rotational Irradiation with three non-coplanar arcs (Rotational Irradiation). For a tumor in the right lung, rotational angles of 220° (from 160° to 20°) for couch angles of 30°, 0° and +30° were applied. For a tumor in the left lung, the arc rotations were diametrically opposite. (b) Static Irradiation with 18 non-coplanar ports (Static Irradiation). Gantry angles of 0°, 30°, 150°, 180°, 210°and 330° for couch angles of −30°, 0° and +30° were used.

Please cite this article in press as: Kunieda E et al., Variation of dose distribution of stereotactic radiotherapy for small-volume lung tumors under different respiratory conditions, Physica Medica (2008), doi:10.1016/j.ejmp.2008.02.002

$$\bar{L}_{eff} = \sum_{i=1}^{n} L_{eff_i}/n \quad (2)$$

where n is the number of beams.

$\bar{L}$ and $\bar{L}_{eff}$ Rotational Irradiation were obtained from lengths or effective lengths calculated per every 10° rotation.

$$\bar{L} = \frac{1}{m \cdot n} \sum_{i,j=1}^{n,m} L_{ij} \quad (3)$$

$$\bar{L}_{eff} = \frac{1}{m \cdot n} \sum_{i,j=1}^{n,m} L_{eff_{ij}} \quad (4)$$

where n is the number of arcs and m = Rotation Angle/10° for each arc.

Dose volume histogram (DVH)

Dose volume histograms (DVH) of the GTV were calculated for each patient under inspiration and expiration conditions for Rotational Irradiation.

Statistical analysis

The t-test was used to compare values for different respiratory conditions. p-values less than 0.05 were considered statistically significant.

Results

In Fig. 3, examples of dose distribution are presented for Rotational Irradiation and Static Irradiation using serial CT data from inspiration. Table 1 indicates path-length, relative electron density, and effective path-length for three breathing conditions (stable-state, inspiration, and expiration breath-hold) according to the irradiation method. Both the mean path-length and mean effective path-length were larger for Static Irradiation than for Rotational Irradiation. In contrast, relative electron density was lower for the former than for the latter. The largest path-length was obtained with inspiration, followed by stable-state and expiration in that order. The difference in mean path-length between inspiration and expiration was 0.5 cm for Rotational Irradiation and 0.6 cm for Static Irradiation. Relative electron density was lower in inspiration than in expiration. Effective path-length was about 0.4–0.5 cm shorter in inspiration than in expiration.

Table 1 Path-length, effective path-length, and relative electron density measured from CT data in three breathing conditions

		Rotational Irradiation	Static Irradiation
Path-length (cm)	Stable-state	9.4 ± 1.8	10.1 ± 1.2
	Inspiration	9.7 ± 1.9	10.6 ± 1.2
	Expiration	9.2 ± 1.8	9.8 ± 1.3
Effective path-length (cm)	Stable-state	5.7 ± 1.3	5.8 ± 1.2
	Inspiration	5.3 ± 1.3	5.5 ± 1.4
	Expiration	5.8 ± 1.3	5.9 ± 1.3
Relative electron density	Stable-state	0.60	0.57
	Inspiration	0.55	0.52
	Expiration	0.63	0.60

Path-length is given as mean ± SD, effective path-length as mean ± SD, and relative electron density as mean. SD, standard deviation.

P values generated from the t-test were used to assess variation of effective path-length in expiration and inspiration ($p = 0.01$ for Rotational Irradiation, $p = 0.03$ for Static Irradiation, both statistically significant).

Table 2 shows required dose at isocenter for 100 MU which was calculated by the FFT convolution and MG superposition algorithms [17] in all three breathing conditions for both types of irradiation procedures. The dose obtained by the FFT convolution algorithm was 7–12% higher than the dose obtained by the MG superposition algorithm. Fig. 4 shows effective path-length and the isocenter dose per 100 MU for each of the nine lesions. Although the isocenter dose obtained by the FFT convolution algorithm linearly decreased relative to effective path-length, there was variation among cases with the MG superposition algorithm.

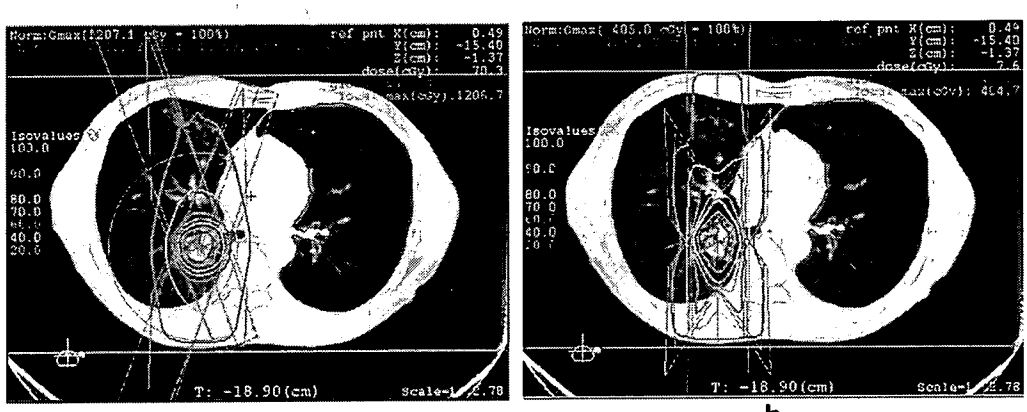

a b

Figure 3 Examples of dose distribution for Rotational Irradiation (a) and Static Irradiation (b).

Please cite this article in press as: Kunieda E et al., Variation of dose distribution of stereotactic radiotherapy for small-volume lung tumors under different respiratory conditions, Physica Medica (2008), doi:10.1016/j.ejmp.2008.02.002

Table 2 The isocenter dose (Gy) per 100 MU calculated with two calculation algorithms in three breathing conditions

		Rotational Irradiation	Static Irradiation
Convolution (Gy)	Stable-state	0.808	0.799
	Inspiration	0.822	0.809
	Expiration	0.803	0.794
Superposition (Gy)	Stable-state	0.745	0.735
	Inspiration	0.743	0.722
	Expiration	0.750	0.738
Superposition/ convolution (%)	Stable-state	0.922	0.920
	Inspiration	0.904	0.892
	Expiration	0.934	0.929

For each patient, integral DVHs for GTV in inspiration and expiration conditions for Rotational Irradiation were obtained, and all DVHs for each patient were averaged (Fig. 5). Although there were no statistical differences in integral DVH obtained by the FFT convolution algorithm between the inspiration and expiration conditions, with the MG superposition algorithm the difference was pronounced. With the latter algorithm, a leftward shift of the integral DVH was noted in inspiration compared with expiration. D_{95} (the minimal dose delivered to 95% of the target volume) for inspiration, stable-state and expiration conditions were 0.878, 0.91 and 0.912 Gy, respectively. D_{75} for inspiration, stable-state and expiration conditions were 0.891, 0.922 and 0.923 Gy, respectively. There were significant differences between inspiration and stable-state, as well as between expiration and inspiration ($p < 0.05$).

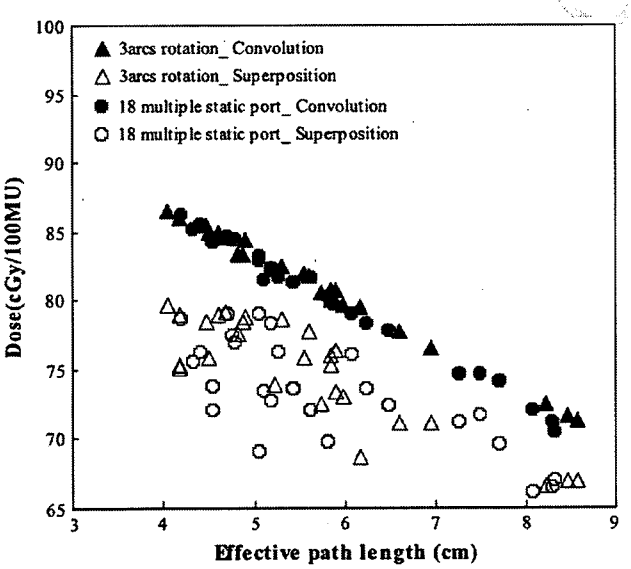

Figure 4 Effective path-length and the isocenter dose calculated by two algorithms (convolution and superposition) plotted for nine tumors in three breathing conditions. Effective path-lengths and the doses were calculated for each static port and averaged. Effective path-lengths and doses for arc irradiations were calculated in the 9 isocenters, each with 3 arcs. The calculations were carried out for each 10° rotation of the gantry and then averaged.

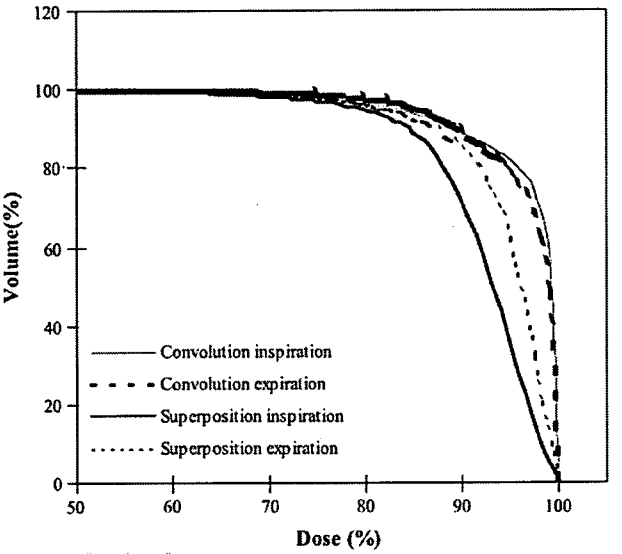

Figure 5 Integral dose-volume histograms (DVHs) for three breathing conditions calculated for Rotational Irradiation with FFT convolution and MG superposition algorithms. DVH curves were obtained for the nine tumors and then averaged.

Discussion

During normal respiration, lung volume typically changes by 20% from 3.3 to 4.1 l on average, as observed in a 10-patient study [18]. However, there are few reports regarding the effect of respiration on the dose distribution of stereotactic radiotherapy for lung tumors.

Our study performed on deep inspiration and expiration conditions indicates that the path-length increased by 2.4–3.7% in stable-state and 5.3–8.7% in inspiration relative to that in the expiration state. Relative electron density decreased by 4.2–4.3% in stable-state and 12.9–13.7% in inspiration relative to expiration.

Although the respiratory conditions were extreme, our results did not indicate large variation in effective path-length under these three respiratory conditions. Obtained effective path-length in inspiration was shorter than that in expiration. These "paradoxical" changes in effective path-length (shorter effective path-length with longer physical path-length) can be easily explained by the expansion of the thoracic cavity with inspiration. However, changes in effective path-length are more complex because the effective path-length is the sum of the product of the path-length in tissue and its electron density. The path-length in the lung increased, whereas electron density decreased, in relation to lung expansion. Our study indicated that the effective path-length decreased in stable-state and inspiration compared with expiration ($p < 0.05$). Observed changes in the path-length, the density and the effective path-length associated with respiratory movement can be expressed as a simplified sphere model.

Please cite this article in press as: Kunieda E et al., Variation of dose distribution of stereotactic radiotherapy for small-volume lung tumors under different respiratory conditions, Physica Medica (2008), doi:10.1016/j.ejmp.2008.02.002

Expiration and inhalation respiratory lung conditions are expressed with small and large spheres, with the radii of the spherical surfaces representing path-lengths (Fig. 6). Because total lung mass is constant, the relationship between path-length and relative electron density in expiration e and inhalation i is expressed using the following equation:

$$\frac{4}{3}\pi L_e^3 \rho_e = \frac{4}{3}\pi L_i^3 \rho_i \quad (5)$$

where L_e and L_i are the path-length of expiration and inspiration, respectively, and ρ_e and ρ_i are relative electron density of expiration and inhalation, respectively.

Because the effective path-length (L_{eff}) is a product of path-length and relative electron density, Eq. (5) can be expressed as

$$(L_e/L_i)^2 = 1/(L_{eff_e}/L_{eff_i}) \quad (6)$$

In this model, relative electron density is inversely proportional to the path-length cubed. Thus, minute changes in path-length may have a great influence on relative electron density. Moreover, this model indicates the effective path-length is inversely proportional to the square of the path-length. A similar deformity of the lung may occur during the inspiration and expiration. Regarding the human chest, respiration is associated with deformity of the thoracic cavity due to diaphragmatic motion and intercostal muscle constriction where the expansion of the lung and thorax or downward movement of the diaphragm during the inspiration are not isotropic. The involvement of diaphragmatic motion in lung respiration is reportedly greater than costal motion [19,20]. In addition, the changes of in path-length and density are expected to be different depending on the beam orientation.

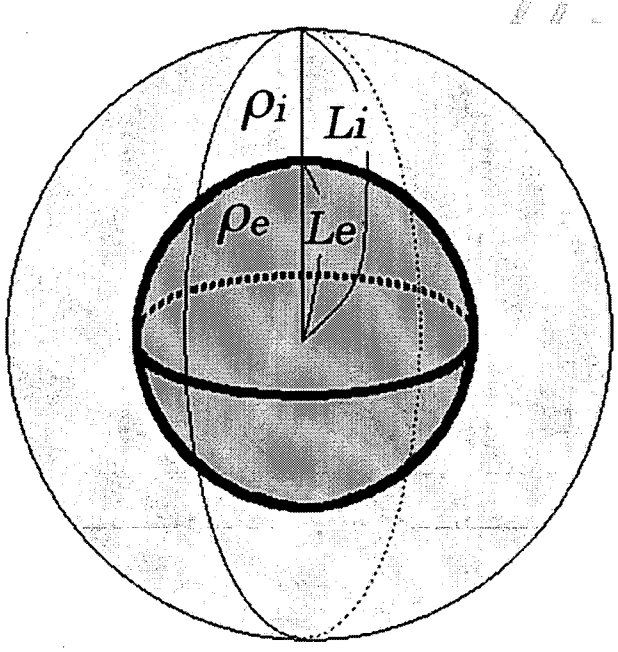

Figure 6 A spherical lung motion model. The inner sphere represents expiration (e) and the outer represents inspiration (i). Radii of the spheres represent path-lengths of expiration and inspiration (L_e, L_i). Relative electron density (ρ_e, ρ_i).

Rotational Irradiation using multiple arcs and Static Irradiation using multiple fields are very common in SRT techniques and selection of the technique depends on the institutional protocols. A comparison of path length, effective path length and relative electron densities between Rotational Irradiation and Static Irradiation for different respiratory conditions are shown in Table 1. Although the effective path lengths for these two irradiation techniques were very similar, there was approximately a 5% difference in electron density between the two techniques. With Rotational Irradiation, longer path-lengths were noted. Interestingly, the impact of these differences on dose/100 MU among different respiratory conditions was negligible (Table 2). However, the isocenter doses per 100 MU delivery were less with the MG superposition calculation than with FFT convolution. The ratios of MG superposition to FFT convolution doses were also indicated in Table 2. The ratios were low in the inspiration phase both with Rotational and Static Irradiation. The lower ratio of MG superposition to FFT convolution doses with inspiration phase can be explained by the difference of the algorithms, as discussed below and the lower lung density in the inspiration phase.

A comparison of the isodose distributions between Rotational Irradiation and Static Irradiation with non-conformal fields is shown in Fig. 3. Rotational Irradiation provides a graphically better dose distribution in this case. However, further optimization of the static fields may yield better results. This requires further investigation.

Three-dimensional (3D) dose distributions are calculated with various algorithms using anatomical data obtained by CT scans. In convolution and superposition algorithms, the dose is computed by convolving the total energy released per unit mass (TERMA) at each point in the patient with the energy deposition kernel [21]. The kernel is generated using the Monte Carlo (MC) particle transport calculation, and it can be divided into the primary and the scatter component [21,22]. In both dose calculation algorithms, the TERMA is computed from fluence, and 3D dose distributions are calculated by separating the energy diffusion process into a primary dose convolution and a scatter dose convolution. Beam attenuation related to the density of the medium is an intrinsic factor to calculate released energy (primary and scatter) associated with the TERMA. Kernel hardening correction factors are computed and applied to the TERMA based on the KERMA (kinetic energy released per unit mass) to TERMA ratio at each depth and at the surface [23,24]. Tissue inhomogeneities cause the greatest distortion of the energy deposition kernels and of the resultant dose distribution compared with those calculated in the water phantom. Therefore, in the MG superposition algorithm, a density scaling method based on O'Connor's theorem [25] is used to scale the kernels by calculating the average density along the straight-line path between the dose deposition and the interaction voxels [17]. However, there are reported differences in the calculated dose of 10% or more among various algorithms [26,27]. Because of the reason mentioned above, the MG superposition algorithm is preferred to FFT convolution, which might result in underdosage of the lung tumor by almost 10% [17,27,28].

Please cite this article in press as: Kunieda E et al., Variation of dose distribution of stereotactic radiotherapy for small-volume lung tumors under different respiratory conditions, Physica Medica (2008), doi:10.1016/j.ejmp.2008.02.002

In the FFT convolution algorithm, kernels remain invariant over the entire space in which they are applied [17]; therefore, the dose/MU decreases linearly with increasing effective path length, which can be seen in Fig. 4. The MG superposition algorithm, however, shows less of a relationship between dose/MU and effective depth. Small effective depths may require the same dose/MU as much larger effective depths. This can be attributed to the kernels accounting for the 3D variations in electron density in the patient [17], for example the lack of lateral electronic equilibrium.

The DVH for GTV, which was calculated in inspiration, stable-state and expiration conditions for Rotational Irradiation, varied depending on the dose calculation algorithm in use. When the MG superposition method was used, a leftward shift of DVH was found in inspiration, in which relative electron density was smaller than that in expiration. The reason for this may be explained from the facts that in the MG superposition algorithm, the density of material between the interaction and dose deposition points is taken into account [17]. For a small lung tumor with different adjacent lung densities, ranges of secondary electrons will be different. Lung density with inspiration will give a longer range of the secondary electrons than with the expiration; therefore, inspiration condition will have a lower electronic equilibrium and dose coverage in the target than the expiration condition.

This study has shown that differences in lung densities in between inspiration and expirations are significant. For small lung tumors the planned dose distributions can change with the breathing phase and the algorithm. In the case of the MG superposition algorithm a better dose homogeneity in the GTV can be achieved when irradiation is done in the expiration phase compared to the inspiration phase, whereas the phase of breathing has very little effect on the planned dose distributions when the FFT convolution algorithm is used. The use of breathing adapted techniques, such as breath-hold or synchronized irradiation, is also important to reduce the planning target volume for stereotactic lung irradiations.

Acknowledgement

We express our gratitude to David McKay, Medical Physicist, Oncology Service, Christchurch Hospital, Christchurch, New Zealand for his kind advice and cooperation in the preparation of this manuscript.

References

[1] Lax I, Blomgren H, Naslund I, Svanstrom R. Stereotactic radiotherapy of malignancies in the abdomen. Methodological aspects. Acta Oncol 1994;33:677–83.
[2] Blomgren H, Lax I, Naslund I, Svanstrom R. Stereotactic high dose fraction radiation therapy of extracranial tumors using an accelerator. Clinical experience of the first thirty-one patients. Acta Oncol 1995;34:861–70.
[3] Nagata Y, Takayama K, Matsuo Y, Norihisa Y, Mizowaki T, Sakamoto T, et al. Clinical outcomes of a phase I/II study of 48 Gy of stereotactic body radiotherapy in 4 fractions for primary lung cancer using a stereotactic body frame. Int J Radiat Oncol Biol Phys 2005;63:1427–31.
[4] Onishi H, Araki T, Shirato H, Nagata Y, Hiraoka M, Gomi K, et al. Stereotactic hypofractionated high-dose irradiation for stage I nonsmall cell lung carcinoma: clinical outcomes in 245 subjects in a Japanese multiinstitutional study. Cancer 2004;101:1623–31.
[5] Haedinger U, Krieger T, Flentje M, Wulf J. Influence of calculation model on dose distribution in stereotactic radiotherapy for pulmonary targets. Int J Radiat Oncol Biol Phys 2005;61:239–49.
[6] Saitoh H, Fujisaki T, Sakai R, Kunieda E. Dose distribution of narrow beam irradiation for small lung tumor. Int J Radiat Oncol Biol Phys 2002;53:1380–7.
[7] Takeda A, Kunieda E, Shigematsu N, Hossain DM, Kawase T, Ohashi T, et al. Small lung tumors: long-scan-time CT for planning of hypofractionated stereotactic radiation therapy—initial findings. Radiology 2005;237:295–300.
[8] Lagerwaard FJ, Van Sornsen de Koste JR, Nijssen-Visser MR, Schuchhard-Schipper RH, Oei SS, Munne A, et al. Multiple "slow" CT scans for incorporating lung tumor mobility in radiotherapy planning. Int J Radiat Oncol Biol Phys 2001;51:932–7.
[9] van Sornsen de Koste JR, Lagerwaard FJ, Nijssen-Visser MR, Graveland WJ, Senan S. Tumor location cannot predict the mobility of lung tumors: a 3D analysis of data generated from multiple CT scans. Int J Radiat Oncol Biol Phys 2003;56:348–54.
[10] de Koste JR, Lagerwaard FJ, de Boer HC, Nijssen-Visser MR, Senan S. Are multiple CT scans required for planning curative radiotherapy in lung tumors of the lower lobe? Int J Radiat Oncol Biol Phys 2003;55:1394–9.
[11] Starkschall G, Forster KM, Kitamura K, Cardenas A, Tucker SL, Stevens CW. Correlation of gross tumor volume excursion with potential benefits of respiratory gating. Int J Radiat Oncol Biol Phys 2004;60:1291–7.
[12] Underberg RW, Lagerwaard FJ, Slotman BJ, Cuijpers JP, Senan S. Use of maximum intensity projections (MIP) for target volume generation in 4DCT scans for lung cancer. Int J Radiat Oncol Biol Phys 2005;63:253–60.
[13] Underberg RW, Lagerwaard FJ, Cuijpers JP, Slotman BJ, van Sornsen de Koste JR, Senan S. Four-dimensional CT scans for treatment planning in stereotactic radiotherapy for stage I lung cancer. Int J Radiat Oncol Biol Phys 2004;60:1283–90.
[14] Keall PJ, Mageras GS, Balter JM, Emery RS, Forster KM, Jiang SB, et al. The management of respiratory motion in radiation oncology report of AAPM Task Group 76. Med Phys 2006;33:3874–900.
[15] Mackie TR, Scrimger JW, Battista JJ. A convolution method of calculating dose for 15-MV x rays. Med Phys 1985;12:188–96.
[16] Ahnesjo A. Collapsed cone convolution of radiant energy for photon dose calculation in heterogeneous media. Med Phys 1989;16:577–92.
[17] Miften M, Wiesmeyer M, Monthofer S, Krippner K. Implementation of FFT convolution and multigrid superposition models in the FOCUS RTP system. Phys Med Biol 2000;45:817–33.
[18] Biancia CD, Yorke E, Chui CS, Giraud P, Rosenzweig K, Amols H, et al. Comparison of end normal inspiration and expiration for gated intensity modulated radiation therapy (IMRT) of lung cancer. Radiother Oncol 2005;75:149–56.
[19] Walsh JM, Webber Jr CL, Fahey PJ, Sharp JT. Structural change of the thorax in chronic obstructive pulmonary disease. J Appl Physiol 1992;72:1270–8.
[20] Krayer S, Rehder K, Vettermann J, Didier EP, Ritman EL. Position and motion of the human diaphragm during anesthesia-paralysis. Anesthesiology 1989;70:891–8.
[21] Mackie TR, Bielajew AF, Rogers DW, Battista JJ. Generation of photon energy deposition kernels using the EGS Monte Carlo code. Phys Med Biol 1988;33:1–20.

Please cite this article in press as: Kunieda E et al., Variation of dose distribution of stereotactic radiotherapy for small-volume lung tumors under different respiratory conditions, Physica Medica (2008), doi:10.1016/j.ejmp.2008.02.002

[22] Boyer AL. Relationship between attenuation coefficients and dose-spread kernels. Radiat Res 1988;113:235–42.
[23] Hoban PW, Murray DC, Round WH. Photon beam convolution using polyenergetic energy deposition kernels. Phys Med Biol 1994;39:669–85.
[24] Hoban PW. Accounting for the variation in collision kerma-to-terma ratio in polyenergetic photon beam convolution. Med Phys 1995;22:2035–44.
[25] O'Connor JE. The variation of scattered x-rays with density in an irradiated body. Phys Med Biol 1957;1:352–69.
[26] Engelsman M, Damen EM, Koken PW, van't Veld AA, van Ingen KM, Mijnheer BJ. Impact of simple tissue inhomogeneity correction algorithms on conformal radiotherapy of lung tumours. Radiother Oncol 2001;60:299–309.
[27 Nishio T, Kunieda E, Shirato H, Ishikura S, Onishi H, Tateoka K. Dosimetric verification in participating institutions in a stereotactic body radiotherapy trial for stage I non-small cell lung cancer: Japan Clinical Oncology Group trial (JCOG0403). Phys Med Biol:In press.
[28] Miften M, Wiesmeyer M, Kapur A, Ma CM. Comparison of RTP dose distributions in heterogeneous phantoms with the BEAM Monte Carlo simulation system. J Appl Clin Med Phys/Am Coll Med Phys 2001;2:21–31.

Please cite this article in press as: Kunieda E et al., Variation of dose distribution of stereotactic radiotherapy for small-volume lung tumors under different respiratory conditions, Physica Medica (2008), doi:10.1016/j.ejmp.2008.02.002

Int. J. Radiation Oncology Biol. Phys., Vol. 70, No. 4, pp. 1057–1065, 2008

0360-3016/08/$–see front matter

ELSEVIER

doi:10.1016/j.ijrobp.2007.07.2383

CLINICAL INVESTIGATION **Lung**

POSSIBLE MISINTERPRETATION OF DEMARCATED SOLID PATTERNS OF RADIATION FIBROSIS ON CT SCANS AS TUMOR RECURRENCE IN PATIENTS RECEIVING HYPOFRACTIONATED STEREOTACTIC RADIOTHERAPY FOR LUNG CANCER

ATSUYA TAKEDA, M.D., PH.D.,*† ETSUO KUNIEDA, M.D., PH.D.,†‡ TOSHIAKI TAKEDA, M.D.,† MICHIO TANAKA, M.D., PH.D.,§ NAOKO SANUKI, M.D.,* HIROFUMI FUJII, M.D., PH.D.,‖ NAOYUKI SHIGEMATSU, M.D., PH.D.,‡ AND ATSUSHI KUBO, M.D. PH.D.‡

*Department of Radiology, Ofuna Chuo Hospital Ofuna, Tokyo, Japan; Departments of †Radiology and §Pathology, Tokyo Metropolitan Hiroo Hospital, Tokyo, Japan; ‡Department of Radiology, Keio University, Tokyo, Japan; and ‖Functional Imaging Division, National Cancer Center Hospital East, Tokyo, Japan

Purpose: To retrospectively analyze opacity changes near primary lung cancer tumors irradiated by using hypofractionated stereotactic radiotherapy (HSRT) to determine the presence or absence of tumor recurrence.
Methods and Materials: After review-board approval for a retrospective study, we examined data from 50 patients treated with curative intent for proven or highly suspected localized peripheral-lung cancer and followed up for at least 12 months. All patients had received 50 Gy in five fractions (80% isodose) and were followed up monthly with chest X-ray until clinical and X-ray findings stabilized. Follow-up computed tomography scans were performed 1 and 3 months after HSRT and thereafter at 3-month intervals during the first 2 years.
Results: Median follow-up was 30.4 months (range, 12.0–73.8 months). Abnormal opacities that were suspicious for recurrent tumor appeared in 20 patients at a median of 20.7 months (range, 5.9–61.4 months). Only 3 patients were finally found to have recurrence; 14 were recurrence free but were suspected to have fibrosis, and findings for the other 3 patients were considered equivocal because of a short follow-up period (≤6 months).
Conclusion: Radiation fibrosis, which may occur 1 year or longer after completion of HSRT, is difficult to distinguish from tumor recurrence. Even when opacities increase on follow-up radiologic scans, recurrence cannot be diagnosed conclusively based on image findings; biopsy occasionally is warranted. © 2008 Elsevier Inc.

Stereotactic radiotherapy, Radiation fibrosis, Computed tomography.

INTRODUCTION

Delivery of a high dose of radiation by using hypofractionated stereotactic radiotherapy (HSRT) often results in radiopacity within the boundaries of a tumor, which would be considered tumor progression. To our knowledge, no study to date evaluated morphologic changes in tumors after HSRT, and only a few reports focused on HSRT-induced lung injuries (1–3).

Complete disappearance of the tumor is rarely seen during follow-up of patients with lung cancer with HSRT. As in many cases, after conventional radiotherapy, the primary tumor may be obscured by postradiation change. A degree of tumor shrinkage usually is observed, and a variety of radiologic patterns that may reflect modifications caused by irradiation also is seen (1, 3). In patients with a good response, tumor opacities usually shrink and thereafter appear as scar-like or linear patterns that persist on radiologic follow-up images. We generally consider these radiologic patterns to reflect tumor control. However, there are cases in which opacities are only minimally reduced in size. Moreover, diagnostic difficulty is often encountered when trying to determine whether the patterns reflect tumor recurrence or mass-like fibrosis after radiotherapy (4, 5). In patients who are candidates for such salvage treatments as surgery, cryoablation (6), and radiofrequency ablation (7), it is essential to diagnose recurrence as early as possible because the smaller the tumor, the easier it is to treat. For example, an adequate size for cryoablation of lung tumors is less than 3 cm in diameter (6). Needless to say, it is important to establish standards for determining tumor recurrence after HSRT to appropriately assess its treatment outcome.

Reprint requests to: Etsuo Kunieda, M.D., Ph.D., Department of Radiology, Keio University, Shinjuku, Tokyo 160-8582, Japan. Tel: (+81) 3-3353-1211 ext. 62531; Fax: (+81) 3-3359-7425; E-mail: kunieda-mi@umin.ac.jp

Conflict of interest: none.
Received May 22, 2007, and in revised form June 28, 2007. Accepted for publication July 20, 2007.

In this study, we retrospectively reviewed follow-up computed tomography (CT) studies of 50 patients obtained during a period of at least 1 year after HSRT for localized peripheral primary lung cancer. Our goal was to analyze opacity changes in the vicinity of irradiated tumors to determine whether there was tumor recurrence.

METHODS AND MATERIALS

Patients

Our institutional review boards approved this study and waived the need for informed consent based on the retrospective design. The study group was composed of 50 patients who underwent HSRT with curative intent for proven or highly suspected localized primary lung cancer located in the periphery of the lung. One case was located in segment 1 + 2 of the left lung and invasion to the aortic arch was noted; however, no patient with thoracic wall invasion was included. All were treated at Institute A ($n = 40$) or Institute B ($n = 10$) from Feb 2001 to March 2006 and were followed up for at least 12 months. There were 30 men and 20 women with a median age of 77 years (range, 56–91 years). Histopathologic type was adenocarcinoma in 31 patients, squamous cell carcinoma in 10, and small-cell carcinoma in 1. In the other 8 patients, early lung cancer was highly suspected, but could not be confirmed histopathologically. Classification as highly suspected lung cancer required at least one of the following criteria: successive tumor growth on CT images, increase in tumor marker level, or positive ^{18}F fluorodeoxyglucose (FDG) positron emission tomography (PET) scan result. Primary lesions were staged as T1 in 30 patients, T2 in 15 patients, and T4 in 1 patient. In the remaining 4 patients, HSRT was administered for treatment of postoperative recurrence. The patient with Stage T4 had a solitary localized tumor not exceeding 4 cm in diameter; however, it involved the aortic arch. None of the patients included in this study showed lymph node involvement or distant metastases before treatment. For the majority of patients, surgery was contraindicated because of advanced age, poor pulmonary function, or the existence of comorbidity. Four patients preferred HSRT despite the feasibility of surgery. Patient background characteristics are listed in Table 1.

Table 1. Patient characteristics and treatments

Characteristics	*n* (%)
Gender	
Male	30 (60.0)
Female	20 (40.0)
Age (y)	
50–59	1 (2.0)
60–69	8 (16.0)
70–79	24 (48.0)
80–	17 (34.0)
T Stage	
T1	30 (60.0)
T2	15 (30.0)
T4	1 (2.0)
Recurrence	4 (8.0)
Pathology	
Adenocarcinoma	31 (62.0)
Squamous cell carcinoma	10 (20.0)
Small-cell carcinoma	1 (2.0)
Unproven (highly suspected)	8 (16.0)
Reason for inoperable	
Old age	12 (24.0)
Refusal	4 (8.0)
Emphysema	12 (24)
Postoperation	3 (6.0)
Other reason	19 (38.0)

Treatment planning and procedure

Treatment planning CT and all treatment procedures were performed with the patient immobilized by using a Vac-Lok immobilization system (Medtec, Orange City, IA). The isocenter was equated to the center of the tumor based on determination using a CT simulator (CT port; Toshiba, Tokyo, Japan, or REXXAM; GE Yokogawa Medical Systems, Tokyo, Japan) at the time of treatment planning and at each radiation treatment. We performed eight-arc dynamic conformal stereotactic radiotherapy with or without additional static conformal ports. The same three-dimensional radiation treatment planning system (XiO, version 4.2; CMS, St. Louis, MO) was used in both institutions. Radiation doses were calculated by using a superposition algorithm with heterogeneity correction.

Gross tumor volume was defined as the visible tumor on CT images using a CT number window level of −600 and width of 1,500. All series equated gross tumor volume to the clinical target volume. To account for breathing motion changes in tumor position, a long-scan-time CT or "slow CT" (6–8 s/slide) was performed to directly delineate internal target volume (8). For planning target volume (PTV), individualized treatment margins of 5–8 mm around the internal target volume were applied. The prescribed dose was defined as the 80% isodose of the maximum dose to ensure that the PTV received at least an 80% isodose of the maximum dose. All 50 patients underwent HSRT with delivery of 50 Gy in five fractions (80% isodose) during 5 to 8 days.

Radiographic follow-up

All patients were followed up monthly on an outpatient basis with chest X-ray examinations until clinical and X-ray findings stabilized. The CT scans were performed at 1 and 3 months after HSRT and thereafter at 3-month intervals during the first 2 years, even in the absence of clinical symptoms. Afterward, CT scans were obtained at 4- to 6-month intervals. The CT examination interval varied slightly depending on the patient's clinical status. If suspicious opacities were seen on periodic radiography, additional CT scans were obtained between scheduled examinations. Single-slice helical CT of the whole chest without contrast material was performed using the following scanning parameters: slice thickness, 10 mm; pitch, 1; tube voltage, 120 kV; tube current, 200 mA; and scan time, 0.75 s/slice. Images focusing on tumors and associated pneumonitis were obtained by means of helical scanning with the following parameters: slice thickness, 2 mm; pitch, 1; tube voltage, 120 kV; tube current, 250 mA; and scan time, 0.75 s/slice. High-resolution CT images were reconstructed by using a high-spatial-resolution algorithm. A 10-mm collimated study was performed for the entire chest, and subsequent images were obtained at 2-mm collimation to cover the tumor and associated postirradiation change. A diagnostic radiologist (T.T.) and radiation oncologist (A.T.) reviewed all CT images. If there was a discrepancy in interpretation between the two observers, they discussed the images to reach a consensus.

If there was a possibility that local treatment or systemic therapy would be required for suspected tumor recurrence, PET using FDG was additionally performed to assess localized findings (extension of locally recurring lesions) and detect distant metastases. Biopsy or surgery was performed if necessary.

RESULTS

Median follow-up was 30.4 months (range, 12.0–73.8 months). Excluding radiologic patterns typical of radiation pneumonitis that occurred 2 to 7 months after radiotherapy, abnormal opacities suspected of being recurrent tumors appeared in 20 patients (Fig. 1). Median time between completion of HSRT and a radiologically recognizable increase in tumor opacity was 20.7 months (range, 5.9–61.4 months). The remaining 30 patients were judged to have achieved tumor control because tumor opacities diminished and ultimately transformed to scar-like or linear patterns.

Of 20 patients initially suspected of having recurrent tumors, 3 (Group A) were ultimately judged to have a recurrence; 2 had a histopathologically proven recurrence, and in the other patient, recurrence was diagnosed based on an opacity growth and increase in tumor marker level. Times to definitive diagnosis of post-HSRT recurrence in the 3 patients were 5.9, 9.2, and 12.0 months, respectively. Fourteen patients (Group B) were judged to be recurrence free, although tumor opacities increased during follow-up and recurrence previously had been suspected. In these cases, median time between completion of HSRT and appearance of an increase in tumor opacity was 21.4 months (range, 8.6–35.6 months). Recurrence was ruled out in 4 patients who were confirmed pathologically to be recurrence free based on surgical biopsy in 1 (Fig. 2), transbronchial lung biopsy in 1, and CT biopsy in 2. In 7 other patients, tumor opacities shrank during follow-up (Fig. 3). In the remaining 3 patients, no subsequent increase in tumor opacity was seen. Opacities were stable for at least 6 months after suspicion of tumor recurrence, and there were no clinical findings suggestive of recurrence (Figs. 4 and 5). The final 3 patients (Group C) were judged to have equivocal findings on April 28, 2007, the last time for data to be included in study analysis, because follow-up periods after increases first seen in tumor opacity were less than 6 months.

In summary, the increased opacities seen during follow-up of 20 patients were classified into three groups: Group A, recurrent tumor; Group B, controlled tumor; or Group C, equivocal findings (Fig. 1; Table 2). Of 14 patients in Group B who were judged to be recurrence free despite an increase in tumor opacity, mass-like dense consolidations corresponding to increased tumor opacities were confined to the lung fields in 9 patients (Figs. 2–4), to both lung fields and subcutaneous tissue on the thoracic wall in 2 patients, and to subcutaneous tissue on the thoracic wall alone in 1 patient. Dense consolidations were seen in the 2 remaining patients: Given lesion locations, obstructive pneumonitis involving the peripheral area could not be ruled out for these 2 patients (Fig. 5).

Of 42 patients with primary lung cancer histopathologically diagnosed, abnormal opacities suspected of recurrence appeared in 16 patients. Two were judged to have recurrence: one was biopsy proven, whereas the other was clinically diagnosed through an increase in tumor marker levels. Twelve patients were considered to be recurrence free: three were confirmed pathologically and the diagnosis was made in others by radiologic follow-up. The remaining 2 patients had equivocal results.

Four patients underwent PET imaging to rule out recurrence when tumor opacities increased. Maximum standard uptake values (SUVmaxs) in these patients were 2.2, 2.8, 3.1, and 5.0 (Table 2). Three patients with relatively low SUVmaxs were finally judged to have achieved tumor control based on other grounds; 2 were pathologically recurrence free, and the remaining tumor shrank during follow-up (Fig. 4). In the fourth patient, who had the highest SUVmax, tumor opacities continued to increase and there were suspicious clinical findings, ultimately leading to a diagnosis of recurrent tumor.

In 1 patient who underwent surgery (Fig. 2), pathologic examination showed sporadic cells with enlarged atypical

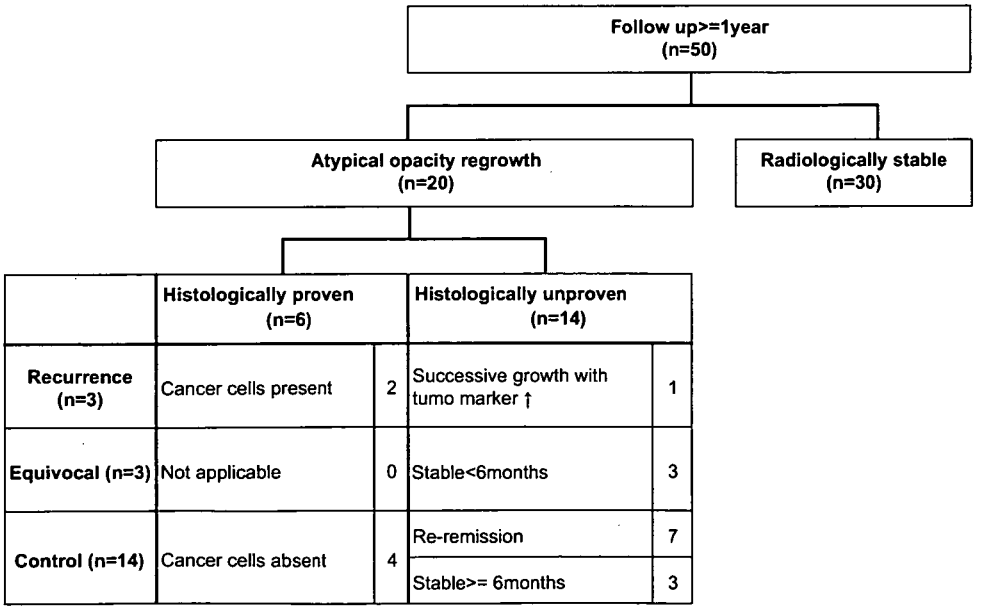

Fig. 1. Flow chart of follow-up schedule after hypofractionated stereotactic radiotherapy.

Fig. 2. Transverse computed tomography (CT) images obtained after hypofractionated stereotactic radiotherapy (HSRT) for highly suspected lung cancer in a 79-year-old man with a lung nodule in the left lower lobe. (a–d) Transverse CT images obtained before and 3, 6, and 9 months after completion of HSRT, respectively. Nodule enlargement was seen 6 and 9 months after completion of HSRT, raising suspicion of local recurrence. The nodule was then resected. (e) Enlargement of the irradiated lung field (Elastica-Masson stain). A tumor-like fibrous scar 7 mm in diameter is seen in the peripheral area 1.5 mm from the pleura, and there is a relatively sharply defined area of fibrosis around the scar. Pleural thickening is minimal with mild wrinkling. (f) Low-power photomicrograph of pulmonary fibrosis around the tumor-like scar (Elastica-Masson stain). Dense fibrosis and fragments of fine elastic fibers of alveolar septa are seen in the area of the tumor-like fibrous scar. Small amounts of fibrin exudate are also evident. Proliferation of elastic fibers of alveolar walls and moderate intra-alveolar fibrosis correspond to pulmonary fibrosis. A large area of fibrosis within the pleural cavity is seen in the area adjacent to healthy lung tissue, but not in tissue affected by pulmonary fibrosis. There is no prominent destruction of the alveolar wall. Fibrous myointimal thickening of small vessels and stenosis of the lumen are marked.

nuclei, possibly attributable to irradiation in the mass-like scar and pulmonary fibrous areas, but there was no evidence of cancerous cells. Furthermore, lymphocytes and plasmacytes had markedly infiltrated the pulmonary fibrous site and the area around the tumor, suggesting that secondary inflammatory changes took place in association with fibrosis. The CT biopsies and/or bronchoscopies were conducted for the remaining 3 patients, who were proved to be recurrence free. Degenerative and fibrous tissues associated with irradiation were observed.

DISCUSSION

Careful follow-up reading of radiologic images from patients treated with HSRT showed that radiologic patterns seen after HSRT are likely to differ from those appearing after conventional radiotherapy. An earlier report found that radiation-induced lung injury occurred during the first year after HSRT (2). The conduction of longer term follow-up of radiologic patterns after HSRT is showing many cases in which it is difficult to determine whether residual opacities reflect viable malignant cells. Therefore, the current study was designed to retrospectively review follow-up CT scans of 50 patients during at least 1 year after HSRT for proven or highly suspected lung cancer in relation to the presence or absence of signs of recurrence.

Timing of radiation-induced fibrosis

In this study, the time between completion of HSRT and demonstrable radiologic increases in tumor opacities in patients in Group B (diagnosed as recurrence free after these increases) and in Group C (equivocal opacities) ranged from 8.6–61.4 months. This timing is believed to correspond to the development of radiation fibrosis. Furthermore, at 1 year or later, radiation fibrosis was detected in 76.5% of patients (13 of 17 patients), as listed in Table 2. In general, radiation-induced fibrosis or solid contraction reportedly occurred at least 3 months after completion of conventional radiotherapy (9, 10) and stabilized 9–12 months after the radiotherapy (11). Previous findings regarding radiation-induced changes during the first year after HSRT showed that opacity shrinkage indicative of radiation injury developed within 6–11 months after completion of HSRT;

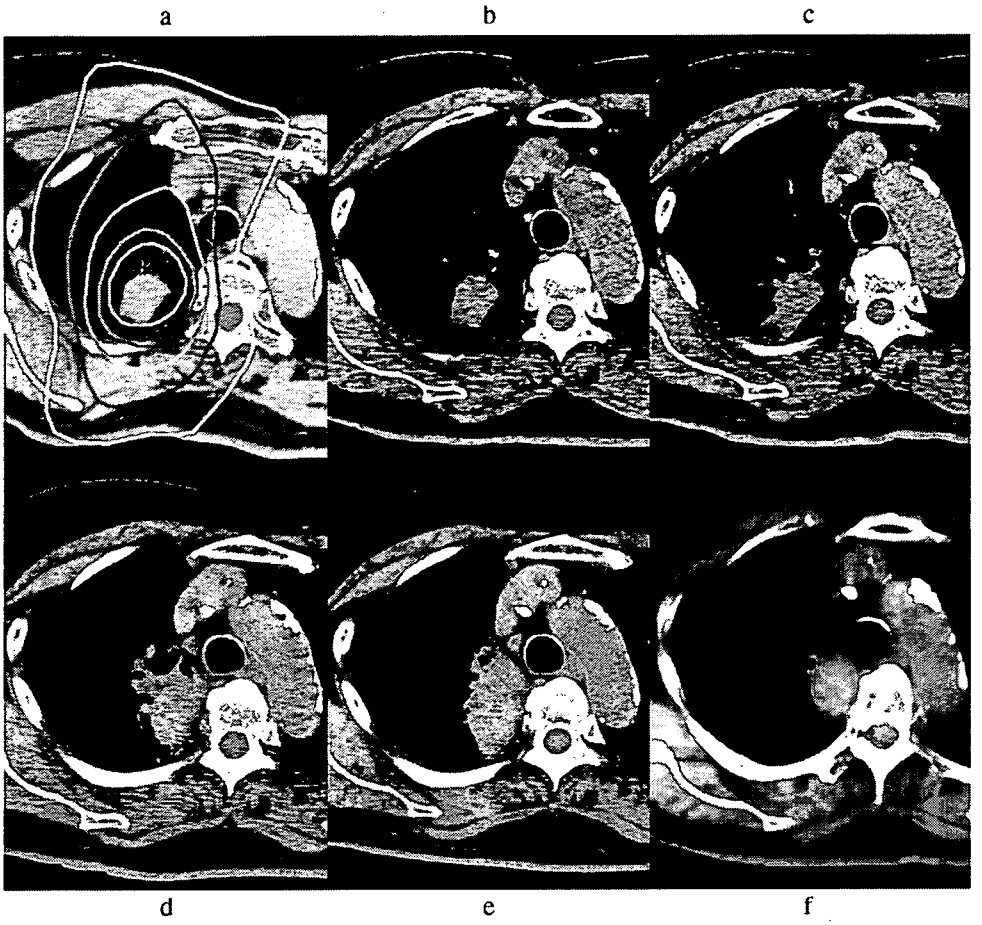

Fig. 3. Transverse computed tomography images obtained after hypofractionated stereotactic radiotherapy (HSRT) in an 80-year-old woman with adenocarcinoma of the right upper lobe. (a) Pre-HSRT image with isodose lines. The red line is the 80% isodose curve and corresponds with planning target volume (PTV). (b–f) Images were obtained at 1, 3, 6, 9, and 23 months after completion of HSRT. Solid consolidations gradually enlarged between 3 and 9 months, raising suspicion of local recurrence. However, opacities diminished 23 months after completion of HSRT.

thereafter, pulmonary opacities were stable on CT images (2). However, longer follow-up showed that radiation fibrosis after HSRT occurred in many patients after a year or more.

These data are consistent with reports that radiation fibrosis may occur more than 1 year after completion of radiotherapy. Timmerman and Wulf (12) reported a patient with SRT-induced fibrosis that became prominent 15 months after treatment, but thereafter disappeared. Their images corresponded to definitions of radiation fibrosis to which we referred in our studies. Another report in which onset of radiation fibrosis was not described stated that mass-like fibrosis appeared in 8 of 19 patients followed up for a mean of 19 months after three-dimensional conformal radiotherapy with 70.0–90.3 Gy in 33–42 fractions, and differentiation of evolving mass-like fibrosis from a recurrent tumor can be particularly difficult (4). In a Phase II study conducted by Timmerman *et al.* (13), an increase in localized opacity was visualized as an abnormal CT sign in the vicinity of irradiated tumors in 17 of 70 patients, but only 3 of these 17 were confirmed by biopsy to have local recurrence. In our study, 20 of 50 patients were suspected of having recurrent tumors. Of these 20 patients, 3 had local recurrence diagnosed. Our results are equivalent with those obtained by Timmerman *et al.* (13) in terms of the ratio of the number of patients suspected to have recurrence to the total number of patients and in terms of the incidence of local recurrence. Thus, the prevalence of radiation fibrosis seen in our experience appears to agree with the reported incidence of increasing opacity without local recurrence confirmed by means of biopsy.

Appearance of radiation fibrosis after HSRT

Our study showed that radiation fibrosis often appeared in normal lung tissue around tumor shrinking opacity and without former severe radiation pneumonitis. Therefore, it is very difficult to differentiate radiation fibrosis from recurrence. In conventional radiotherapy, radiation fibrosis is a secondary occurrence to severe radiation pneumonitis (9, 10). Radiation fibrosis typically manifests as traction bronchiectasis, volume loss, and scarring (14), and during the first year after HSRT, we found that the shift of severe radiation pneumonitis to radiation fibrosis corresponded to a steep dose distribution close to the PTV (2).

In addition, the observation that opacities of radiation fibrosis often shrank several months after HSRT was not reported previously. It is important for clinicians to recognize that temporary opacity size increases caused by radiation

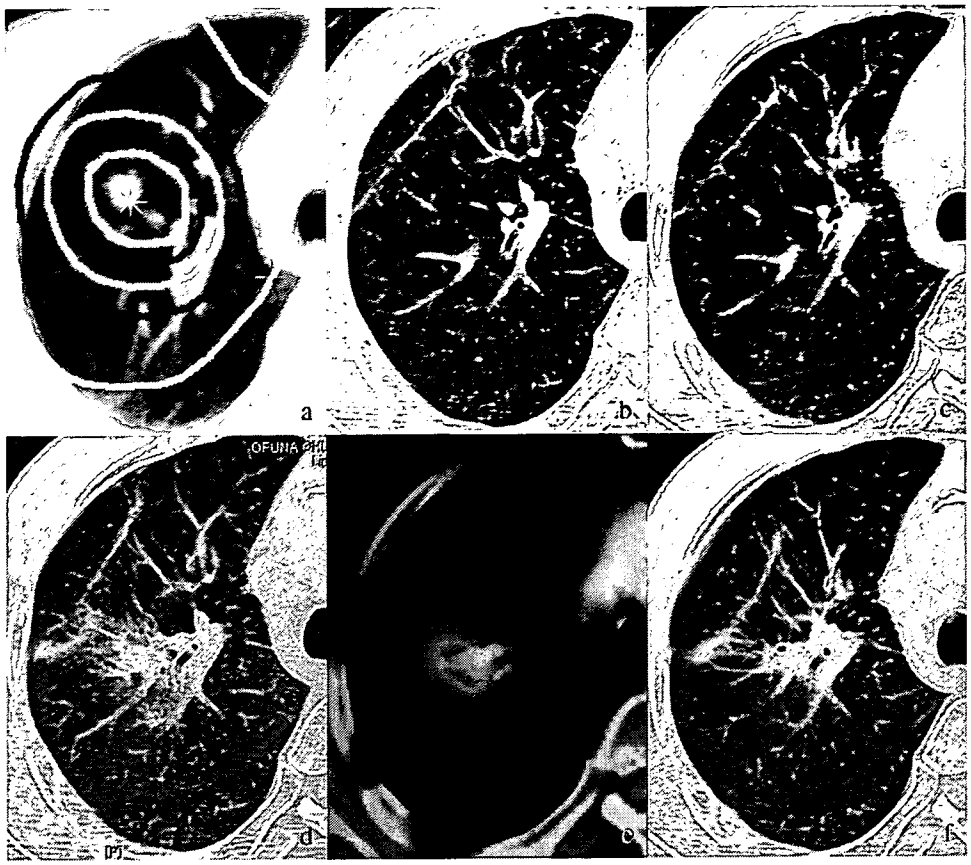

Fig. 4. Transverse computed tomography (CT) images and a positron emission tomography (PET)-CT image after hypofractionated stereotactic radiotherapy (HSRT) in an 83-year-old man with adenocarcinoma of the right upper lobe. (a) Pre-HSRT image with dose isodose lines. The red line is the 80% isodose curve and corresponds to planning target volume (PTV). (b–f) Transverse CT images obtained at 19, 22, and 25 months; PET-CT image at 26 months; and transverse CT images at 34 months after completion of HSRT. The solid opacity had enlarged at 25 months after completion of HSRT. Thus, PET-CT was performed to rule out recurrence in the PTV vicinity and showed increased activity (maximum standard uptake value, 3.13) corresponding to the opacity. The solid opacity observed was indicative of local recurrence. However, it diminished 34 months after completion of HSRT.

fibrosis can develop during the follow-up of patients treated with HSRT to avoid prematurely diagnosing recurrent tumors. To our knowledge, this is the first report describing radiation fibrosis after HSRT.

Radiobiologic analysis

The radiation dose we prescribed for the 80% isodose area was 50 Gy in five fractions. Biologic effectiveness dose in the PTV for acute tumor effect and the chronic normal tissue effect were calculated as 100–140 Gy_{10} and 216.7–322.9 Gy_3 when α/β values were assumed to be 10 and 3, respectively. Although the demarcated solid pattern mostly appeared at the PTV region and adjacent area, in some cases, it appeared at the peripleural or hilar regions, which were within the 60% isodose area.

Other possible causes of a demarcated solid pattern

A few other mechanisms may explain the demarcated solid pattern in addition to radiation fibrosis. At a high daily dose, HSRT is associated with a clear component of bronchial injury. Such bronchial injury occurs as a result of atelectasis of "downstream" lung tissue, although the area is minimally exposed to radiation (15). Furthermore, airway damage occurs relatively late, *i.e.*, 9–12 months after completion of radiotherapy, and consists of collapse of the lumen with subsequent downstream atelectasis and fibrosis (16). In our experience with 2 patients with lesions that showed demarcated solid patterns, it was difficult to distinguish radiation fibrosis from atelectasis of downstream lung tissue, and both components may have been present (Fig. 5).

Follow-up CT and FDG-PET examinations after radiotherapy for lung cancer

It is often difficult to distinguish radiation fibrosis from local recurrence and other events on CT images. When radiologically atypical manifestations of radiation-induced lung injury are observed, the possibility of infection, locally recurrent neoplasm, lymphangitis, and carcinomatosis should be considered (14). Filling-in of radiation therapy–induced bronchiectatic change (17, 18) and opacity with a convex lateral border (18) reportedly are typical radiologic signs of recurrent tumor. However, these signs were not always indicative of recurrence in this study. One possible explanation is that radiation fibrosis induced by HSRT is so dense that

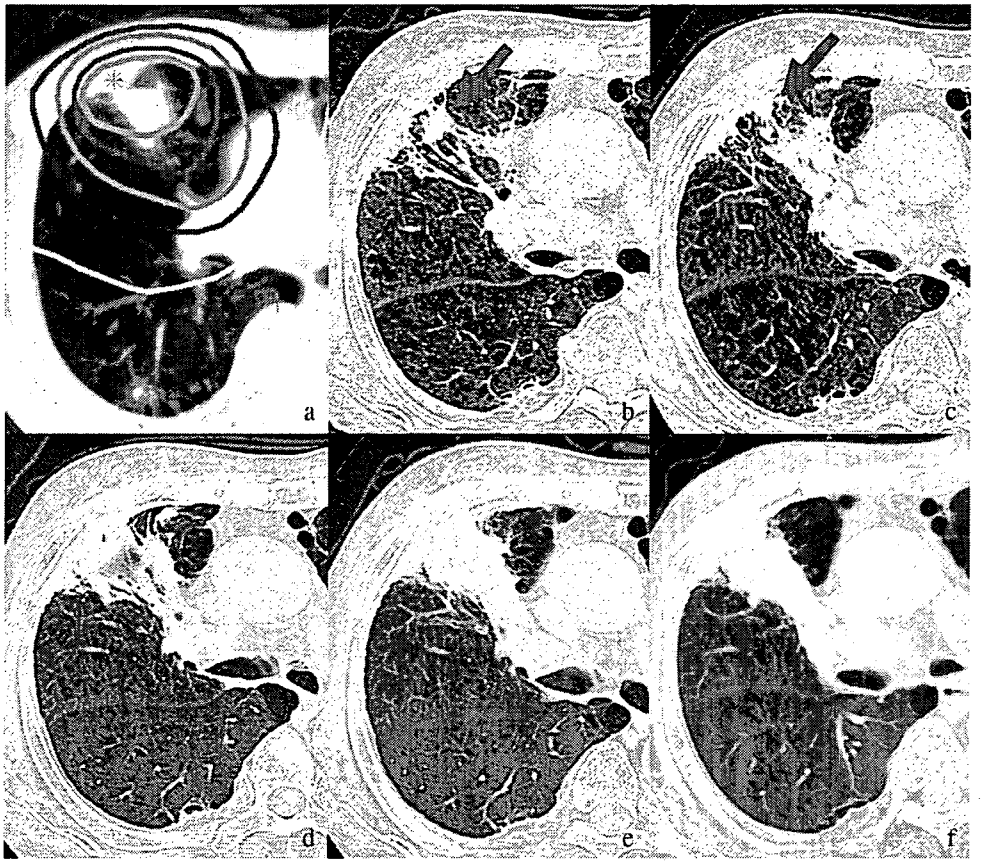

Fig. 5. Transverse computed tomography (CT) images after hypofractionated stereotactic radiotherapy (HSRT) for highly suspected lung cancer in a 91-year-old man with a nodule in the right upper lobe. (a) Pre-HSRT image with isodose lines. The red line is the 80% isodose curve and corresponds to planning target volume (PTV). (b–f) Transverse CT images obtained at 13, 16, 19, 21, and 29 months after completion of HSRT. A linear shadow and bronchial traction appeared upstream from the tumor. Both gradually expanded into a solid opacity suggestive of obstructive pneumonia, radiation fibrosis, or hilar lymph node recurrence. However, the opacity was apparently stable between 21 and 29 months after HSRT. However, the tumor opacity at the periphery (arrow) gradually diminished. The solid lesion grew downward and obscured the diminished tumor opacity.

bronchiectatic changes would have been obscured at first appearance of fibrosis or on follow-up radiologic scans.

Patz *et al.* (19) studied 43 patients with abnormal chest radiographic findings after radiotherapy for bronchogenic carcinoma by using FDG-PET to differentiate recurrent or persistent tumors from fibroses. In their study, sensitivity and specificity of FDG-PET for detecting recurrent tumors (SUV > 2.5) were 97.1% and 100%, respectively; the SUV for recurrent tumors was significantly higher than that for fibrosis. In an FDG-PET study conducted by Inoue *et al.* (20) involving 38 patients, the investigators concluded that a threshold SUV of 5.0 provided optimal diagnostic accuracy for detecting recurrence. However, Hoopes *et al.* (21) showed that a substantial proportion of patients who underwent HSRT had a moderately increased SUV at 12 months, but there was no evidence of local failure on subsequent follow-up scans. Additional studies are needed regarding the role of PET for distinguishing recurrences from postradiation changes in a large number of patients and using modern PET technology.

In our study, PET examination was performed in only 4 patients, too few to allow conclusions about the significance of FDG-PET findings to be drawn.

If additional treatment is possible, even at the time recurrence is detected, early diagnosis is critical. In such cases, we consider biopsy or surgery to be an essential diagnostic tool. However, patients should be carefully followed up for a longer time when an alternative treatment modality is not clearly available.

Limitations

Limitations of this study include its retrospective design and small sample size. In addition, there were only a few cases in which pathologic confirmation or PET imaging findings were available. In patients showing diminished opacities, we were unable to confirm whether the patients were malignancy free. Longer post-HSRT follow-up of patients is required to elucidate the ramifications of temporary increases in opacity size.

CONCLUSION

In conclusion, it should be noted that radiation fibrosis, which may occur 1 year or more after completion of

Table 2. Patient with suspected recurrent tumor

Patient no.	T	Pathology	Status	Shape classification	Reason	Period of growth after SRT (M)	PET SUVmax
1	2	Adenocarcinoma	Recurrence	Solid	Biopsy	5.9	
2	1	Squamous cell carcinoma	Free	Chest wall	Biopsy	8.6	2.8
3	1	Highly suspicious	Recurrence	Solid	Biopsy	9.2	
4	1	Highly suspicious	Free	Solid	Surgery	9.6	
5	1	Adenocarcinoma	Free	Solid	Diminished	10.3	
6	1	Highly suspicious	Equivocal	Solid	—	11.3	
7	1	Adenocarcinoma	Recurrence	Solid	Successive growth	12.0	5.0
8	2	Squamous cell carcinoma	Free	Solid	Diminished	14.0	
9	2	Highly suspicious	Free	Downstream	Stable	15.7	
10	2	Adenocarcinoma	Free	Solid	Diminished	17.0	
11	1	Adenocarcinoma	Equivocal	Solid	—	20.7	
12	1	Squamous cell carcinoma	Free	Solid + chest wall	Diminished	20.9	
13	rec	Adenocarcinoma	Free	Solid	Diminished	21.9	
14	1	Adenocarcinoma	Free	Solid	Biopsy	22.3	
15	2	Squamous cell carcinoma	Free	Downstream	Diminished	23.7	
16	1	Adenocarcinoma	Free	Solid	Diminished	24.6	3.13
17	2	Adenocarcinoma	Free	Solid	Stable	28.8	
18	1	Adenocarcinoma	Free	Solid	Stable	32.6	
19	1	Adenocarcinoma	Free	Solid + chest wall	Biopsy	35.6	2.2
20	1	Adenocarcinoma	Equivocal	Solid	—	61.4	

Abbreviations: M = months; SRT = stereotactic radiotherapy; PET = positron emission tomography; SUVmax = maximum standard uptake value.

HSRT, is difficult to distinguish from tumor recurrence. Even when opacities increase on follow-up radiologic scans and high uptake is noted on FDG-PET scans, recurrence cannot be conclusively diagnosed based on image findings of increased opacities and high metabolism on PET scans. Biopsy occasionally is still warranted.

REFERENCES

1. Aoki T, Nagata Y, Negoro Y, *et al.* Evaluation of lung injury after three-dimensional conformal stereotactic radiation therapy for solitary lung tumors: CT appearance. *Radiology* 2004;230: 101–108.
2. Takeda T, Takeda A, Kunieda E, *et al.* Radiation injury after hypofractionated stereotactic radiotherapy for peripheral small lung tumors: Serial changes on CT. *AJR Am J Roentgenol* 2004;182:1123–1128.
3. Kimura T, Matsuura K, Murakami Y, *et al.* CT appearance of radiation injury of the lung and clinical symptoms after stereotactic body radiation therapy (SBRT) for lung cancers: Are patients with pulmonary emphysema also candidates for SBRT for lung cancers? *Int J Radiat Oncol Biol Phys* 2006;66:483–491.
4. Koenig TR, Munden RF, Erasmus JJ, *et al.* Radiation injury of the lung after three-dimensional conformal radiation therapy. *AJR Am J Roentgenol* 2002;178:1383–1388.
5. Wulf J, Hadinger U, Oppitz U, *et al.* Stereotactic radiotherapy of targets in the lung and liver. *Strahlenther Onkol* 2001;177: 645–655.
6. Kawamura M, Izumi Y, Tsukada N, *et al.* Percutaneous cryoablation of small pulmonary malignant tumors under computed tomographic guidance with local anesthesia for nonsurgical candidates. *J Thorac Cardiovasc Surg* 2006;131:1007–1013.
7. Fernando HC, De Hoyos A, Landreneau RJ, *et al.* Radiofrequency ablation for the treatment of non-small cell lung cancer in marginal surgical candidates. *J Thorac Cardiovasc Surg* 2005;129:639–644.
8. Takeda A, Kunieda E, Shigematsu N, *et al.* Small lung tumors: Long-scan-time CT for planning of hypofractionated stereotactic radiation therapy—Initial findings. *Radiology* 2005;237: 295–300.
9. Libshitz HI, Southard ME. Complications of radiation therapy: The thorax. *Semin Roentgenol* 1974;9:41–49.
10. Libshitz HI, Brosof AB, Southard ME. Radiographic appearance of the chest following extended field radiation therapy for Hodgkin's disease. A consideration of time-dose relationships. *Cancer* 1973;32:206–215.
11. Gross NJ. Pulmonary effects of radiation therapy. *Ann Intern Med* 1977;86:81–92.
12. Timmerman R, Wulf J. Stereotactic radiotherapy of lung tumors. In: Slotman B, Solberg T, Verellen D, editors. Extracranial stereotactic radiotherapy and radiosurgery. Bristol, PA: Taylor & Francis; 2006. p. 197–230.
13. Timmerman R, McGarry R, Yiannoutsos C, *et al.* Excessive toxicity when treating central tumors in a phase II study of stereotactic body radiation therapy for medically inoperable early-stage lung cancer. *J Clin Oncol* 2006;24:4833–4839.
14. Choi YW, Munden RF, Erasmus JJ, *et al.* Effects of radiation therapy on the lung: Radiologic appearances and differential diagnosis. *Radiographics* 2004;24:985–998.
15. Timmerman R, Lohr F. Normal tissue dose constraints applied in lung stereotactic body radiation therapy. In: Kavanagh B, Timmerman R, editors. Stereotactic body radiation therapy. Philadelphia: Lippincott Williams & Wilkins; 2005. p. 29–37.

16. Kavanagh BD, McGarry RC, Timmerman RD. Extracranial radiosurgery (stereotactic body radiation therapy) for oligometastases. *Semin Radiat Oncol* 2006;16:77–84.
17. Libshitz HI, Sheppard DG. Filling in of radiation therapy-induced bronchiectatic change: A reliable sign of locally recurrent lung cancer. *Radiology* 1999;210:25–27.
18. Bourgouin P, Cousineau G, Lemire P, *et al.* Differentiation of radiation-induced fibrosis from recurrent pulmonary neoplasm by CT. *Can Assoc Radiol J* 1987;38:23–26.
19. Patz EF Jr., Lowe VJ, Hoffman JM, *et al.* Persistent or recurrent bronchogenic carcinoma: Detection with PET and 2-[F-18]-2-deoxy-D-glucose. *Radiology* 1994;191:379–382.
20. Inoue T, Kim EE, Komaki R, *et al.* Detecting recurrent or residual lung cancer with FDG-PET. *J Nucl Med* 1995;36:788–793.
21. Hoopes DJ, Fletcher J, Tann M, *et al.* A prospective trial of serial FDG-PET in patients with medically inoperable stage 1 non-small lung cancer treated with Hypofractionated stereotactic body radiotherapy (SBRT) [Abstract]. *Int J Radiat Oncol Biol Phys* 2006;66(Suppl.):S25–S26.

Hepatology Research 2008; 38: 60–69 doi: 10.1111/j.1872-034X.2007.00084.x

Original Article

Hypofractionated stereotactic radiotherapy with and without transarterial chemoembolization for small hepatocellular carcinoma not eligible for other ablation therapies: Preliminary results for efficacy and toxicity

Atsuya Takeda,[1,2] Masahiko Takahashi,[3]* Etsuo Kunieda,[2,4] Toshiaki Takeda,[2] Naoko Sanuki,[1] Yuji Koike,[3†] Kazuhiro Atsukawa,[5] Toshio Ohashi,[4] Hidetsugu Saito,[6] Naoyuki Shigematsu[4] and Atsushi Kubo[4]

[1]*Department of Radiology, Ofuna Chuo Hospital, Kanagawa, Departments of* [2]*Radiology and* [3]*Internal Medicine, Hiroo Metropolitan General Hospital, Tokyo, Departments of* [4]*Radiology and* [6]*Internal Medicine, Keio University, Tokyo, and* [5]*Department of Internal Medicine, Hiratsuka Municipal Hospital, Kanagawa, Japan*

Aim: To investigate the efficacy and toxicity of hypofractionated stereotactic radiotherapy for the treatment of patients presenting with hepatocellular carcinoma (HCC) in a single institutional setting.

Methods: Sixteen patients who presented with solitary HCC, including two patients with a tumor thrombus of the portal veins, were treated with stereotactic radiotherapy with or without transarterial chemoembolization. The criteria for stereotactic radiotherapy were existence of technical difficulties for other ablation therapies, inoperable disease or refusal to undergo surgery, tumor staged as Grade A or B according to the Child–Pugh classification, and solitary tumor distant from the gastrointestinal tract and kidney with a tumor volume <100 cm^3. In 14 of 16 patients, a total dose of 35–50 Gy was delivered in 5–7 fractions over 5–9 days.

Results: At the end of a mean follow-up of 612 days (median 611 days; range 244–994 days), all patients were alive. Eight of 16 patients had complete responses and seven others were judged as stable with lipiodol accumulation. In one patient, local recurrence developed after 489 days. Intrahepatic recurrences developed outside the treated volume in six patients and no extrahepatic metastases developed during follow-up. No serious treatment-related toxic manifestations developed.

Conclusions: Stereotactic radiotherapy for HCC with or without transarterial chemoembolization is feasible therapy and provides good local control with a short treatment period. Stereotactic radiotherapy may be of clinical benefit in patients who are inoperable or for whom there are difficulties in other ablation therapies.

Key words: ablation therapy, hepatocellular carcinoma, liver damage, stereotactic radiotherapy, transarterial chemoembolization

INTRODUCTION

THE INCIDENCE OF hepatocellular carcinoma (HCC) is increasing in Japan,[1] the USA,[2] and other countries.[3,4] Because hepatitis B and C virus infections are associated with a high risk of HCC, it has been recommended that high-risk infected patients be monitored regularly by ultrasound scanning and tumor marker testing to detect HCC at an early stage.[5,6] Surgery has limited utility in the treatment of HCC because the underlying cirrhosis and the presence of multiple simultaneous lesions often contraindicate it.[7,8] In addition, HCC frequently recurs even after apparently successful curative resection[9] because of multifocal development arising from viral infection. Less invasive ablative techniques, such as percutaneous ethanol injection therapy (PEIT)[10–15] and radiofrequency ablation (RFA)[16,17] are often utilized.

Although some recent reports indicated favorable results with 3-D conformal irradiation or proton beam treatments,[18–23] radiotherapy has not been considered a frontline treatment of HCC because of the toxicity

Correspondence: Dr Etsuo Kunieda, Department of Radiology, Keio University, Shinjuku, Tokyo 160-8582, Japan. Email: kunieda-mi@umin.ac.jp

Present addresses: *Department of Internal Medicine and †Department of Emergency and Critical Care Medicine, Keio University, Tokyo, Japan.

Received 12 January 2007; revision 8 February 2007; accepted 13 February 2007.

observed in patients treated with doses to the entire liver as low as 30–35 Gy with conventional (e.g. 2 Gy/day) fractionation, which is usually an insufficient dose for curative treatment of HCC.[24,25] However, the highest tolerated dose of radiation is highly dependent on the volume of liver irradiated,[26–29] such that a small volume of liver can tolerate higher doses of radiation without serious hepatic injury.

Hypofractionated, stereotactic radiotherapy enables accurate delivery of high doses of radiation to a specific lesion with a short treatment period. This technique was initially developed for the brain, and has since been applied to extracranial lesions. Blomgren *et al.* first reported the successful use of hypofractionated, stereotactic, high-dose radiation therapy for the treatment of extracranial malignancies, including hepatic tumors,[30] and other investigators have reported similar favorable results.[31–35] The purpose of our study was to investigate the efficacy and toxicity of hypofractionated, stereotactic radiotherapy for the treatment of patients presenting with HCC who had not been previously exposed to other forms of ablation therapy.

METHODS

Patient selection

IN OUR INSTITUTION, Hiroo Metropolitan General Hospital, the first choice for treatment for a small, solitary HCC lesion is local ablation using RFA or PEIT. When these options are limited by technical difficulties and the patient is inoperable or refuses surgery, we recommend the combination therapy of transarterial chemoembolization (TACE) and stereotactic radiotherapy. The area just below the hepatic dome and adjacent to the main portal vein is particularly susceptible to complications with other local ablation therapies. Other indications for the use of stereotactic radiotherapy are technical difficulties with other ablation therapies, tumors staged as Grade A or B according to the Child–Pugh classification, and a solitary tumor distant from the gastrointestinal tract and kidney with a tumor volume <100 cm^3.

The study protocol was reviewed and approved by our Institutional Review Board. Written informed consent was obtained from all patients enrolled in the study before they underwent the procedure.

Patient characteristics

Based on our selection criteria, we performed stereotactic radiotherapy on 16 patients, including two patients with a tumor thrombus in the portal vein, who presented with HCC at the Hiroo Metropolitan General Hospital, between December 2002 and September 2004. Characteristic findings with diagnostic images such as dynamic computed tomography (CT) scans confirmed diagnoses. Risk factors such as HBV hepatitis, HCV hepatitis, or nonalcoholic steatohepatitis (NASH) were noted in all patients except one who received a pathological diagnosis after a prior tumor resection.

Baseline patient characteristics are shown in Table 1. There were 14 men and two women with a median age of 69 years (range 53–78 years), including two patients with chronic hepatitis B and 12 patients with chronic hepatitis C. Fourteen patients were in class A and two were in class B of the Child–Pugh classification. The Cancer of Liver Italian Program scores were 0 in 11 patients, 1 in three patients, and 2 in two patients. HCC lesions were located in segments 7 or 8 in nine patients, in segment 1 in one patient, and adjacent to the main portal vein in four patients. The median tumor volume was 13.6 cm^3 (range 3.4–72 cm^3). The maximum diameter of the tumor was 1.9–7.0 cm.

Stereotactic radiotherapy

Prior to stereotactic radiotherapy, 14 patients underwent TACE to obtain a synergistic local treatment effect as well as to visualize the position of the target with non-contrast-enhanced CT scanning. One patient refused to undergo the procedure and another had a portal thrombosis that precluded its use. After the placement of a catheter, an emulsion of 30–40 mg epirubicin in 3–4 cm^3 iodized lipiodol was infused into the artery that supplied the HCC lesion. Then embolization was induced with a small amount of gelatin sponge particles until the flow of the feeding artery was markedly decreased.

The median time interval between TACE and stereotactic radiotherapy was 13 days (range 5–40 days). When lipiodol in the surrounding tissue obscured the tumor, stereotactic radiotherapy was postponed until it had been washed out. When CT showed only slight accumulation of lipiodol in the tumor, stereotactic radiotherapy was initiated within a few days after TACE.

Patients were immobilized using an individually shaped vacuum pillow. An abdominal band was used to restrict the movement of the abdominal wall and in turn minimize respiratory motion of the liver during CT scanning in preparation for treatment. This abdominal band was used for daily irradiation. After confirming by fluoroscopy that the diaphragmatic motion was less than 1 cm, long-scan-time CT (slow CT) was performed at the rate of 8 s per image to visualize most of the

Table 1 Characteristics of 16 patients undergoing hypofractionated stereotactic radiotherapy for small HCC

Patient no	Age (years)	Sex	Child–Pugh		CLIP score	Risk factor for HCC	GTV (cm^3)	Tumor site	TACE	Radiation treatment			Follow-up (days)	Status
			Class	Score						Total	Fraction	Days		
1	55	M	A	5	0	HCV	3.4	S8	+	50	5	7	994	NED
2	69	F	B	7	2	HCV	10.2	S7/8	+	20	5	7	833	IHR
3	64	M	A	6	2	HCV	32.5	PTT	-	32	8	13	842	NED
4	78	M	A	5	1	HBV	18.2	S5/8	+	40	5	7	727	NED
5	70	M	B	8	1	HBV	13.2	S7/8	+	40	5	7	705	NED
6	57	M	A	5	0	HCV	14.0	S7/8	+	50	5	7	696	NED
7	71	M	A	5	1	HCV	15.2	S7/8	+	35	5	8	568	IHR
8	70	M	A	5	0	HCV	3.4	S7/8	+	35	5	7	548	NED
9	75	F	A	5	0	HCV	9.0	S4	+	40	5	7	518	NED
10	58	M	A	5	0	HCV	67.9	PTT	+	35	5	5	502	NED
11	63	M	A	6	0	HCV	4.1	S1	+	35	5	5	463	IHR
12	64	M	A	5	0	-	5.9	S8	-	40	5	7	413	IHR
13	53	M	A	6	0	HCV	15.7	S3	+	35	5	7	387	IHR
14	76	M	A	5	0	NASH	72.0	S5/6	+	35	5	9	244	NED
15	69	M	A	5	0	HCV	20.0	S5	+	35	7	9	489	LR
16	69	M	A	5	0	HCV	3.5	S7	+	35	5	5	379	NED

CLIP, Cancer of the Liver Italian Program; GTV, gross tumor volume; HCC, hepatocellular carcinoma; HCV, hepatitis C virus; HBV, hepatitis B virus; IHR, intra-hepatic recurrence; LR, local recurrence; NASH, nonalcoholic steatohepatitis; NED, no evidence of disease; PTT, portal tumor thrombosis; TACE, transarterial chemoembolization.

trajectory of tumor movement or internal target volume.[36] A 5-mm margin was added to the internal target volume to define the planning target volume. When the internal target volume was less than 10 cm^3, the margin was increased to 10 mm.

At the daily radiation therapy sessions, long-scan-time CT was performed using a CT simulator (CT port, Toshiba Medical Systems, Tokyo, Japan) in order to determine the isocenter for the daily treatments. The patients were placed on a special wood board and fixed with a customized vacuum-pillow in a manner similar to the CT examination for the treatment planning. They were then fixed with the vacuum-pillow on the board and carried to the treatment couch. Patients were treated by dynamic, conformal, 8-arc irradiation, using a multileaf collimator, planned by a radiation treatment planning system (XiO version 2.7.0; Computerized Medical Systems, St Louis, MO, USA). X-ray beams from a 6 MV linear accelerator (Siemens, Concord, CA, USA) were used. The superposition dose calculation algorithm[37] was used in order to obtain the dose distribution and the target dose.

The treatment plans, including the dose and fraction size, for each patient were approved by a single radiation oncologist (AT). To determine the dose and fraction size the target volume, the dose distribution to the normal liver, and doses to other adjacent organs at risk were considered. Patient conditions such as underlying liver function or prominent ascites were also taken into account. A total dose of 35–50 Gy was planned in 5–7 fractions over 5–9 days except for two patients (Table 1). The treatment was planned to enclose the planning target volume area by the 80% isodose-line, and 80% of the maximum dose was defined as the prescribed dose. The normal tissue dose constraints were that the volume of the liver that received more than 20 Gy in 5 fractions should not exceed 20% of the rest of the liver excluding the gross tumor volume, more than 50% of the hemilateral kidney should not receive 10 Gy in 5 fractions, and any point dose to the duodenum, stomach or bowel should not exceed 25 Gy in 5 fractions.

The patients were seen monthly by a hepatologist (MT, YK, or KA) and by the radiation oncologist (AT), and blood was collected for measurements of aspartate and alanine aminotransferase, total bilirubin, serum albumin, prothrombin time (%), white blood cell and platelet counts, and hemoglobin content. Treatment responses and local recurrences were evaluated with dynamic CT 1 month after treatment and every 3 months thereafter. Dynamic CT scans were carried out over the range of the diaphragmatic dome to the inferior edge of the liver. Images were obtained before the contrast enhancement and 30 s (arterial phase) and 180 s (equilibrium phase) after injection of 100 mL of

non-ionic contrast medium into the arm vein at a rate of 3 mL/s.

Statistical analysis

The local and intrahepatic control rates and overall survival were calculated according to the Kaplan–Meier method. The Wilcoxon test was used to compare the measurements of aspartate and alanine aminotransferase, total bilirubin, serum albumin, white blood cell and platelet counts, and hemoglobin content made before and 4, 8, 12, 24, and 48 weeks after stereotactic radiotherapy. The analyses were carried out with the SPSS 12 software (SPSS, Chicago, IL, USA). $P < 0.05$ was considered statistically significant.

RESULTS

Dose distributions

IN 14 OF 16 patients, a total dose of 35–50 Gy was delivered in 5–7 fractions over 5–9 days. A patient with a portal thrombus (patient 3) was treated with a dose of 32 Gy in 8 fractions over 13 days. The patient who developed ascites secondary to TACE (patient 2) received 20 Gy delivered in 5 fractions over 7 days.

Dose volume histograms (DVH) of the uninvolved liver (liver volume other than the planning target volume) for all patients are presented in Figure 1. The range of mean liver doses was 4.0–15.5 Gy (median 8.6 Gy). The volumes that received more than 10 Gy in the right kidney were 8% of the right kidney in two patients (patients 10 and 14). In those two patients, the mean doses to the right kidney were 2.7 Gy and 4.6 Gy, respectively. In two patients (patients 3 and 15), the maximum doses to the duodenum were 5.2 and 6.6 Gy, respectively. In other patients, doses to the digestive tracts were negligible. The normal tissue dose constraints we adopted prior to the start of our study were satisfied for all patients.

Clinical characteristics, tumor response, and survival

At the end of the mean follow-up of 612 days (median 611 days; range 244–994 days), all patients were alive. A relapse adjacent to the planning target volume developed in one patient 489 days after the treatment. Intrahepatic recurrences developed outside the treated volume in six patients without development of extrahepatic metastases during follow-up. All the intrahepatic recurrences in six patients were at least 2 cm away from the edge of the planning target volume. When no tumor enhancement was detected within the planning target volume on enhanced dynamic CT 6 months or more after treatment, patients were judged as having no relapse. Eight of 16 patients had complete responses with resolution of lipiodol accumulation. In seven other patients, no tumor enhancement was observed with dynamic CT. In these cases, the lesion was judged as stable with lipiodol accumulation inside the tumor. Relapse-free survival and intrahepatic recurrence-free survival are shown in Figure 2.

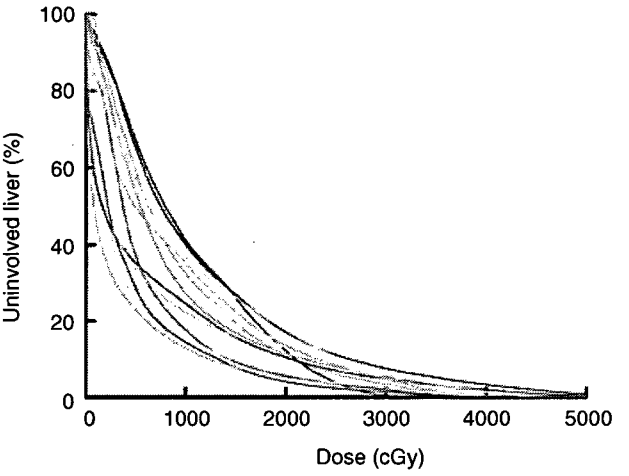

Figure 1 Dose volume histograms of the liver for all patients: absolute dose (cGy) versus percentage volume of uninvolved liver (liver volume other than the planning target volume).

Figure 3 shows representative dynamic CT characteristics before and after treatment. There was a faint early and prolonged enhancement corresponding to the tumor area, including the planning target volume or the high-dose irradiated marginal area, which persisted for several months after irradiation (Fig. 3b). However, this enhancement was clearly distinguishable from the tumor enhancement, which was hypodense in the equilibrium phase compared to the surrounding tissue.

In the patient who underwent stereotactic radiotherapy for the treatment of portal thrombus (patient 3), the size of the tumor thrombus decreased to 20% of the initial volume at 3 months and resolved at 6 months after the treatment. The patient was alive without disease progression 28 months after treatment (Fig. 4).

Although there were no significant changes of the serum tumor markers in the median values for the entire group, in seven patients whose serum alpha-fetoprotein (AFP) was more than 100 ng/mL before the treatment, the AFP level decreased after the treatment ($P = 0.03$) (Fig. 5). In 10 patients whose protein induced by vitamin K absence (PIVKA-II) was more than

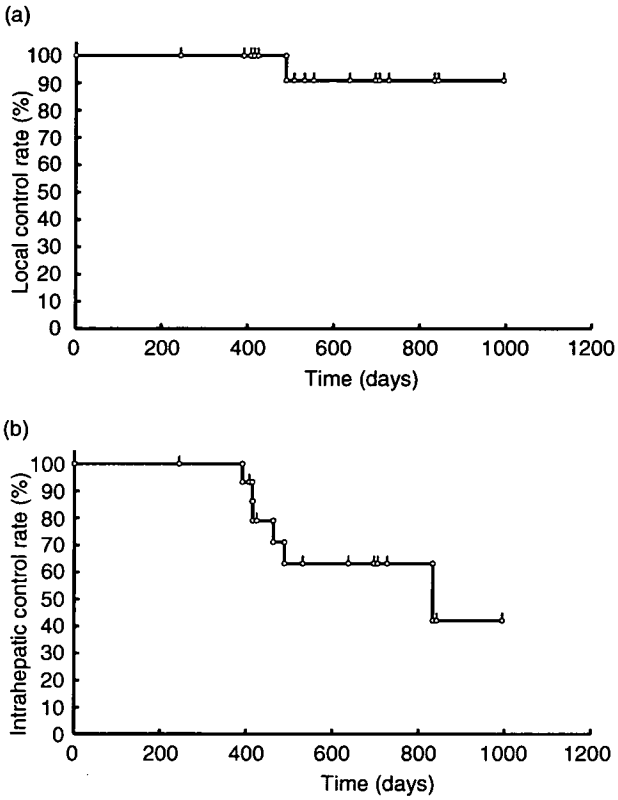

Figure 2 (a) Relapse-free survival and (b) intrahepatic-recurrence-free survival. At the end of a mean follow-up of 612 days all patients were alive.

40 mAU/mL, it significantly decreased after the treatment ($P = 0.007$).

Treatment-related toxicity

All scheduled treatments were completed without manifestations of toxicity other than mild nausea reported by two patients. Serum albumin concentrations and platelet counts often decreased mildly 4 weeks or more after treatment, but they returned to pre-irradiation levels within 24 weeks and 36 weeks, respectively. Aspartate aminotransferase, alanine aminotransferase, total bilirubin, white blood cell counts, and hemoglobin content were not significantly changed by stereotactic radiotherapy. The changes in alanine aminotransferase, albumin, and platelet counts are shown in Figure 6.

The Child–Pugh classification score of patient 4 increased by 4 points (to a score of 9), resulting in a Child–Pugh Grade B, 8 weeks after irradiation due to a decrease in albumin and an increase in total bilirubin concentrations and an increased prothrombin time (Table 2). However, at 48 weeks, the score had decreased by 4 points without any intervention and the patient returned to Grade A. In five other patients, the Child–Pugh score increased transiently by 1 point and in one patient by 2 points. These scores returned to baseline within 48 weeks after irradiation, and the patients developed no serious treatment-related toxic manifestations. In the remaining nine patients, the Child–Pugh scores were unchanged or decreased after stereotactic radiotherapy. One of these patients developed ascites after the stereotactic radiotherapy, which resolved with medical treatment. No patient suffered hepatic encephalopathy.

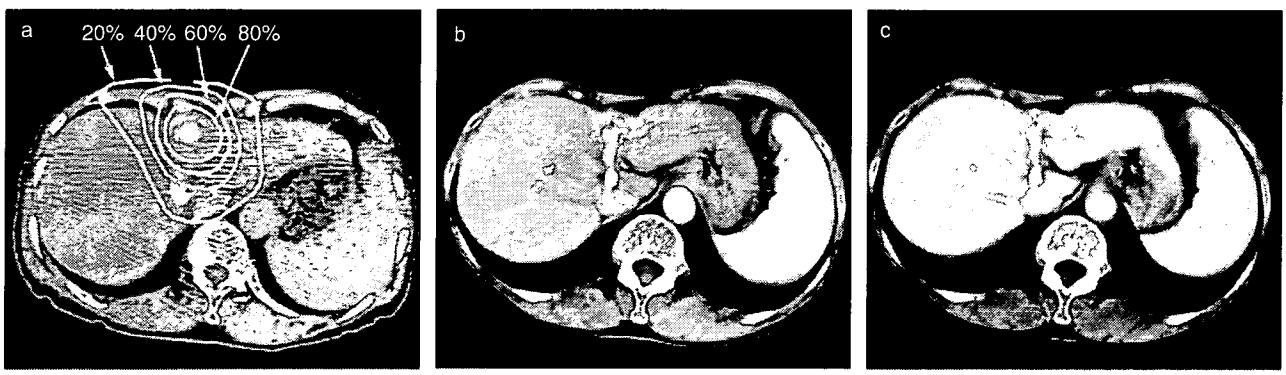

Figure 3 Computed tomography (CT) in patient 9. (a) Lipiodol pooled in the primary lesion before irradiation. The isodose curves for 20%, 40%, 60%, and 80% of the maximum dose are indicated. (b) Arterial phase CT 74 weeks after irradiation. Lipiodol remains pooled and contrast enhancement is observed in the high-dose area surrounding the primary lesion. (c) Portal phase CT 74 weeks after irradiation. Residual contrast enhancement is observed in the area surrounding the tumor. These enhancements are post-irradiation changes.